Optimization of Multi-Bias Electroplating based on Laser-Induced Graphene Seeds for Antenna Applications

Alessio Mostaccio, *Member, IEEE,* Gaetano Marrocco, *Fellow, IEEE*

***Abstract*—Electroplating is a consolidated fabrication technique for antennas, enabling the selective growth of metallic coatings over conductive patterns on conformal substrates. However, when the seed layer exhibits modest conductivity, as in the case of Laser-Induced Graphene (LIG), potential gradients along the cathode cause the deposited thickness to vary with the distance from the bias terminals. The resulting inhomogeneous coating degrades the antenna radiation characteristics relative to the simulated design.**

To address this limitation, this work introduces a combined static–RF optimization methodology that jointly maximizes the uniformity of the electroplated layer and minimizes the RF ohmic losses. The problem is formulated as an iterative minimization algorithm that determines both the minimum number of bias points and their placement along the cathode perimeter, based on the combined DC and RF current distributions.

The methodology is validated on two challenging seed layouts to separately assess deposition uniformity and RF degradation under sub-optimal biasing. Both numerical and experimental results show that, despite the choice of the first bias terminal being critical, the recommended placement of multiple bias points can improve the uniformity of the deposit up to 50%. When applied to a tri-band antenna, the algorithm excludes single-bias configurations, where deposition inhomogeneity and current crowding increase the likelihood of short circuits during deposition, and identifies a three-bias solution that yields RF performance within 1 dB of the bulk-copper counterpart.

***Index Terms*—Antenna, Electroplating, Optimization, Terminal effect, Laser-Induced Graphene**

I. Introduction

Electroplating is a well-established manufacturing technique for the fabrication of antennas and radio-frequency (RF) components [1]. Compared to full-surface metallization, it is more cost-effective and scalable, making it an attractive solution for mass-production [2], [3]. Examples include wideband biconical antennas [4], dielectric resonators with lateral metallic strips [5], dual circularly polarized antennas with bidirectional radiation patterns [6], but also millimeter-wave devices, with tiny intricate metallic details over three-dimensional substrates [7], [8]. More advanced uses of electroplating include multilayer Cu/Co metaconductors to reduce the skin-depth effect and improve radiation efficiency in array of antennas [9], as well as unconventional demonstrations such as a random fractal tree monopole antenna [10].

From a fabrication standpoint, the electrochemical growth of metallic coatings onto dielectric surfaces is enabled by a conductive *seed layer*, which can be patterned with one of the techniques in Table I. Inkjet-, screen-, and 3D-printing are the most straightforward options but have limited spatial resolution, are often incompatible with curved substrates, and may require high sintering temperatures [11], [12], [13]. More advanced techniques, such as aerosol jet printing, electroless plating, and sputtering, provide better resolutions although they rely on costly equipment and chemical reagents that hinder their scalability [14], [15], [7], [8], [9].

TABLE I: Techniques for seed layer patterning on dielectric cathodes

	Resolution $[\mu m]$	Material	Ref.
Inkjet-Printing	$20/50$	Ag/Cu/Graphite	[11]
Screen-Printing	$100/250$	Ag/Graphite	[12]
3D-Printing	$200/300$	Cu	[13]
Aerosol Jet-Printing	$10/20$	Ag/Cu	[14]
Electroless Plating	$5/20$	Ni/Cu	[15]
Sputtering	$\ll 1$	Ti/Ni/Cu	[7]

Recently, Laser-Induced Graphene (LIG) has been proposed as a low-cost and straightforward alternative to pattern conductive seeds [16]. Starting from carbon-rich substrates, a porous graphitic network can be synthesized in a single-step and chemical-free process by leveraging laser irradiation, [17], [18]. The technique enables the synthesis of size- and pattern-controllable layouts with micrometric resolution ($\approx$ 1-10 μm). Furthermore, it avoids any additional surface activation, and combines good electrical conductivity with fast and scalable fabrication. Typical precursor materials include thermoplastic polymers such as Polyimide (PI) or Poly-ether-ether-ketone (PEEK), paper, wood, fabric and even food [17], [18]. To date, LIG electroplating has been predominantly employed for sensing applications [19], [20], [21], [22], and RF resonators [23]. Compared with the aforementioned highly conductive primers, LIG exhibits a much lower electrical conductivity (10^2-10^4 S/m). As a result, the potential along the cathode rapidly drops with the distance from the feeding point (i.e., the *terminal effect* [24], [25]), thus producing non-uniform coatings, as in Fig. 1. This effect becomes even more critical for electroplated antennas, where the potential gradients are amplified by the larger area compared to sensors, and a coating as thick as the skin depth must be ensured [4]. Indeed, if the deposited metal remains thinner than its skin depth, the

Dr. Alessio Mostaccio and Prof. Gaetano Marrocco are with the Pervasive Electromagnetics Lab, University of Tor Vergata, Rome, 00133 Italy, e-mail: alessio.mostaccio@uniroma2.it.

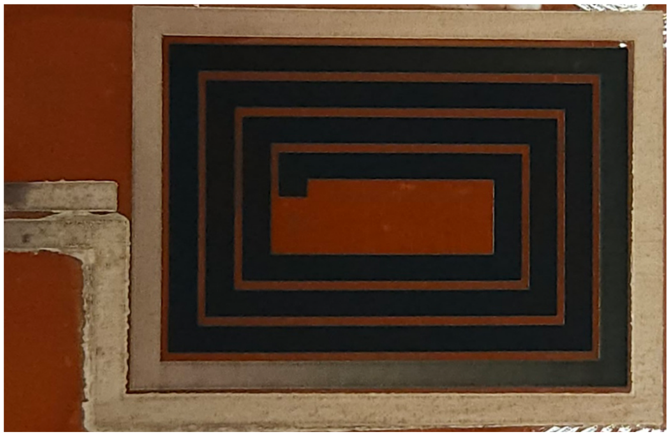

Fig. 1: Example of terminal effect on a LIG seed causing a non-uniform copper-coating of a spiral antenna layout for NFC applications after 2 hours of electrodeposition at 100 mA bias current.

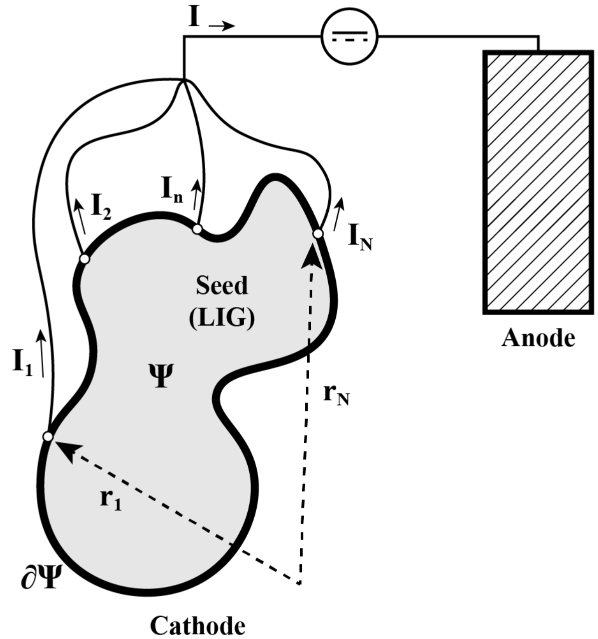

Fig. 2: Schematic representation of the electrical connection of the anode and the LIG cathode (Ψ) to the current generator by means of N biasing nodes, each supplying a current I_n.

RF surface currents are forced through partially conductive regions (i.e., the LIG film), thus increasing the ohmic losses, mismatching the input impedance, and degrading the efficiency [4]. A recent work by the authors further corroborated this concept, showing how the conductivity of LIG seeds affects the electroplating of a flexible UHF RFID antenna [26]. The study experimentally demonstrated that increasing the seed conductivity enhances both the deposition homogeneity and the antenna performance, yet it also reduces the mechanical robustness of the seed and its achievable engraving resolution. Consequently, merely increasing conductivity is not sufficient, and strategies that ensure uniform coatings even with low-conductivity seeds are required.

Several studies have addressed the optimization of electroplating parameters to improve the uniformity of the deposited metal [27], [28], [29], [30], [31]. In resistive seed layers [32], [33], [34], multiple bias points distributed along the cathode perimeter, up to the limit of "full-perimeter contact", have been proposed to reduce potential gradients and enhance coating uniformity. In RF devices, however, thickness uniformity is not the only key point. RF surface currents, indeed, are inherently non-uniform, and different regions contribute unequally to radiation efficiency and impedance matching. Consequently, insufficient plating in high-current areas directly increases ohmic losses, whereas reduced conductivity in low-current regions has only a marginal impact. Maximizing uniformity, therefore, does not necessarily guarantee optimal RF performance and may require unnecessarily complex bias networks. Based on this rationale, this work elevates the selection of the electroplating bias configuration from a pure fabrication step to an RF co-design variable. The proposed joint static-RF optimization framework couples the DC current distribution, driving metal growth, with the RF surface current distribution, governing electromagnetic losses. Hence, the methodology aims at determining the minimum number and placement of bias points required to balance deposition homogeneity and RF efficiency in LIG-seeded antennas, while keeping architectural complexity as low as possible.

The remainder of the paper is organized as follows: Section II revisits the physics of electrochemical deposition on resistive seed layers and establishes the connection between the low-frequency (DC) deposition process and the RF power loss. The section also presents the proposed optimization strategy for determining, iteratively, the favorable number and configuration of the bias points with the purpose of minimizing the ohmic losses of the resulting antenna and maximizing the plating homogeneity. Section III reports an experimental validation carried out on a complex-shaped structure under controlled assumptions. Finally, Section IV provides an application of the method to a multiband IoT antenna, showing how the optimized plating strategy translates into improved electromagnetic performance.

II. Problem Formulation

A. Electroplating representation

Let us consider a conductive seed cathode, made by LIG, of surface Ψ (Fig. 2), that is assumed to work as an antenna or microwave component at frequency f. The anode is a metal with bulk conductivity σ_m and mass density ρ_m. Both the anode and cathode are immersed into a solution containing the ions of the bulk metal. The electrodes are biased by an external DC source by means of N electrodes, at positions $\boldsymbol{r}'_n \in \Psi$, $n = 1, ..., N$. Each node provides a biasing current I_n so that, by neglecting other sources of DC losses, the total current supplied by the external generator, I, is

$$I = \sum_{n=1}^{N} I_n. \tag{1}$$

We hereafter denote with $\boldsymbol{c} = \{(I_1, \boldsymbol{r}_1), ..., (I_N, \boldsymbol{r}_N)\}$, the set of the biasing currents and their application points, respectively.

The DC current density $\boldsymbol{J}_{DC}(\boldsymbol{c}, \boldsymbol{r}, t)$ induced on the LIG cathode is parametrized as

$$\boldsymbol{J}_{DC}(\boldsymbol{c}, \boldsymbol{r}, t) = I\boldsymbol{j}_{DC}(\boldsymbol{c}, \boldsymbol{r}, t) \quad (2)$$

where $\boldsymbol{j}_{DC}(\boldsymbol{c}, \boldsymbol{r}, t)$ is the DC current density on the cathode at time t produced by a unitary input biasing current for the specific configuration $\boldsymbol{c}$.

The deposited mass per unit-area, $m\ [Kg/m^2]$, is related to the current density $\boldsymbol{J}_{DC}(\boldsymbol{c}, \boldsymbol{r}, t)$ and to the biasing duration T by Faraday's law [27]:

$$m(\boldsymbol{c}, \boldsymbol{r}, T) = \frac{M}{zF} I \int_0^T |\boldsymbol{j}_{DC}(\boldsymbol{c}, \boldsymbol{r}, t)|\, dt \quad (3)$$

where M is the molar mass of the deposited metal, z is the number of electrons involved in the process, and $F = 96485\ C/mol$ is the Faraday constant.

Hence, the corresponding local thickness $h(\boldsymbol{c}, \boldsymbol{r}, T)$ of the electroplated layer can be expressed as

$$h(\boldsymbol{c}, \boldsymbol{r}, T) = \frac{m(\boldsymbol{c}, \boldsymbol{r}, T)}{\rho_m} = KI \int_0^T |\boldsymbol{j}_{DC}(\boldsymbol{c}, \boldsymbol{r}, t)| dt \quad (4)$$

where $K = \frac{M}{zF\rho_m}$ is a solution-specific constant, typically provided by the manufacturer. Notably, the biasing current only affects the local thickness of the deposit after a period T without altering the potential distribution, and, thus, the coating homogeneity.

Finally, the resulting sheet resistance $R_s(\boldsymbol{c}, \boldsymbol{r}, T)$ of the electroplated layer is related to the local current density by

$$R_s(\boldsymbol{c}, \boldsymbol{r}, T) = \frac{1}{\sigma_m h(\boldsymbol{c}, \boldsymbol{r}, T)} = \frac{1}{\sigma_m KI \int_0^T |\boldsymbol{j}_{DC}(\boldsymbol{c}, \boldsymbol{r}, t)|\, dt}. \quad (5)$$

Due to the terminal effect, the growth rate of the metal deposit on a lossy seed layer strongly depends on the distance from the feed points: regions close to the bias nodes thicken rapidly, whereas remote or highly resistive areas experience only marginal deposition in the early stages. In these regions, when the local metal layer approaches or falls below the skin depth, residual low-conductivity paths or incomplete coverage introduce additional ohmic losses and surface-roughness-induced scattering, ultimately degrading antenna efficiency and radiation properties. As electroplating continues, the newly formed metal locally reduces the sheet resistance, progressively improving the accessibility of farther regions and modifying the overall current distribution [24], [25]. For a sufficiently long deposition time, the whole cathode surface will eventually be plated. However, if the seed-layer sheet resistance is not uniform, the resulting coating thickness will be markedly inhomogeneous: low-resistance zones grow disproportionately, forming thick ridges, while resistive areas remain thin. In flexible conductors, this uneven overgrowth can generate sharp, stress-amplifying features that severely compromise mechanical robustness, reducing bendability and promoting cracking or delamination under repeated deformation [35], [36]. Moreover, when the cathode layout includes narrow gaps or fine separations between adjacent traces, prolonged exposure significantly increases the likelihood that such gaps become unintentionally bridged by copper particles, as for the spacing between the first two turns of the spiral in Fig. 1. This conductive bridging produces permanent short circuits that irreversibly alter the electrical response of the device, potentially detuning resonances or even rendering the RF structure unusable. These failure mechanisms highlight the importance of maintaining the DC current distribution as uniform as possible during plating, thereby preventing excessively unbalanced growth and minimizing the risk of unintended conductive paths.

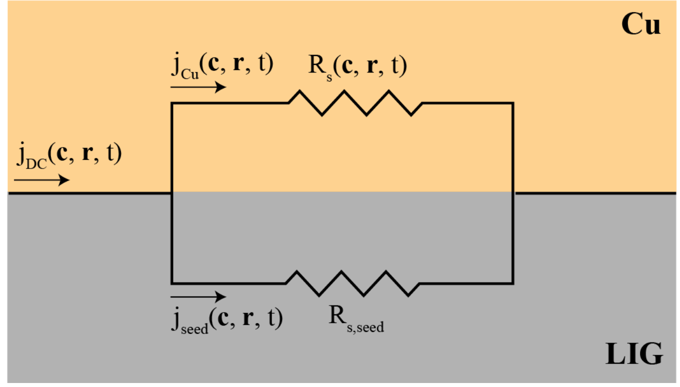

Fig. 3: Equivalent circuit model of the LIG-Cu composite in the early stages of electrodeposition.

Since the goal of this study is to compare different biasing configurations rather than predicting the exact temporal evolution of the deposited layer, the analysis focuses on the early stages of electroplating, i.e., after a short time τ and when only a nanometric layer is formed. At this stage, the sheet resistance of the newly-formed conductive layer (5) is comparable to, or even higher than, that of the LIG seed, $R_{s,seed}$. As a result, the current will flow in the LIG–Cu bilayer through two parallel resistive paths, namely that of the deposit and of the LIG seed (Fig. 3). The composite material is electrically equivalent to a single conductor with an effective sheet resistance, R_p,

$$R_p(\boldsymbol{c}, \boldsymbol{r}, T) = \left(\frac{1}{R_s(\boldsymbol{c}, \boldsymbol{r}, T)} + \frac{1}{R_{s,seed}} \right)^{-1} \quad (6)$$

To simplify the analysis, we consider the condition where the sheet resistance of the deposited metal is comparable to that of the seed, which governs the initial DC current distribution. Let $\boldsymbol{j}_{95} = |\boldsymbol{j}_{DC}(\boldsymbol{c})|_{95\%}$ denote the 95th percentile of the initial distribution of the current density $\boldsymbol{j}_{DC}(\boldsymbol{c}, \boldsymbol{r}, 0)$. The corresponding region $A_{95\%}$, defined so that $r \in A_{95\%}$ if $|\boldsymbol{j}_{DC}(\boldsymbol{c}, \boldsymbol{r}, 0)| > \boldsymbol{j}_{95}$, identifies the areas where the initial current density is the highest. Let us now introduce a characteristic plating time τ; for $T < \tau$, the region $A_{95\%}$ remains poorly plated, so that its sheet resistance can still be approximated by that of the seed

$$R_s(\boldsymbol{c}, \boldsymbol{r}, \tau) \approx R_{s,seed} \quad (7)$$

In the remaining portions of the cathode, where the DC current density will be even lower, the corresponding sheet resistance is higher than that of the seed. Under these conditions, the DC current distribution at time τ can be approximated by that for $t = 0$ [25]:

$$\boldsymbol{j}_{DC}(\boldsymbol{c},\boldsymbol{r},\tau) \approx \boldsymbol{j}_{DC}(\boldsymbol{c},\boldsymbol{r},0) \equiv \boldsymbol{j}_{DC}(\boldsymbol{c},\boldsymbol{r}) \ \forall \ \boldsymbol{r} \in \Psi \tag{8}$$

where $\boldsymbol{j}_{DC}(\boldsymbol{c},\boldsymbol{r})$ is now the solution of an electrostatic problem.

Hence, (5) simplifies to

$$R_s(\boldsymbol{c},\boldsymbol{r},\tau) = \frac{1}{\sigma_m K I |\boldsymbol{j}_{DC}(\boldsymbol{c},\boldsymbol{r})| \tau} \tag{9}$$

The characteristic time τ can be estimated by combining (7) and (9), and the product $KI\tau$ becomes

$$KI\tau(\boldsymbol{c}) = \frac{1}{\sigma_m R_{s,seed} \boldsymbol{j}_{95}} \tag{10}$$

Finally, the sheet resistance of the LIG-Cu composite is computed as

$$R_s(\boldsymbol{c},\boldsymbol{r},\tau) = R_{s,seed}\boldsymbol{j}_{95} \frac{1}{|\boldsymbol{j}_{DC}(\boldsymbol{c},\boldsymbol{r})| + \boldsymbol{j}_{95}} \tag{11}$$

Although the local current distribution progressively evolves as copper is deposited, the preferential growth paths established during the early stage are preserved throughout the process. Consequently, configurations promoting a more uniform current distribution at $t = 0$ are expected to produce more uniform coatings after prolonged deposition.

By assuming the concentration of the cations in the solution as constant, and by neglecting any mass transfer [31], [27], $|\boldsymbol{j}_{DC}(\boldsymbol{c},\boldsymbol{r})|$ is now enforced only by the shape of the cathode, the biasing points, and the conductivity of the LIG trace, σ_{LIG}. The current density can then be expressed through Ohm's law (12) in terms of the electrostatic potential $V(\boldsymbol{c},\boldsymbol{r})$:

$$\boldsymbol{j}_{DC}(\boldsymbol{c},\boldsymbol{r}) = -\sigma_{LIG}\nabla V(\boldsymbol{c},\boldsymbol{r}) \tag{12}$$

$V(\boldsymbol{c},\boldsymbol{r})$ is the solution of the Laplace equation:

$$\nabla \cdot (\sigma_{LIG}\nabla V(\boldsymbol{c},\boldsymbol{r})) = 0, \quad \boldsymbol{r} \in \Psi \tag{13}$$

under the Neumann boundary conditions at the feed points:

$$\sigma_{LIG} \left. \frac{\partial V(\boldsymbol{c},\boldsymbol{r})}{\partial n(\boldsymbol{r})} \right|_{\boldsymbol{r}=\boldsymbol{r}'_n} = -\frac{I_n}{I_{tot}} \quad n = 1,...,N \tag{14}$$

where $\frac{\partial}{\partial n}$ denotes the spatial derivative along the outward normal to the cathode surface.

To quantitatively evaluate the degree of homogeneity produced by the specific configuration $\boldsymbol{c}$, the *coefficient of variation*, CV, is introduced:

$$CV(\boldsymbol{c}) = \frac{std\,(\boldsymbol{j}_{DC}(\boldsymbol{c},\boldsymbol{r}))}{< \boldsymbol{j}_{DC}(\boldsymbol{c},\boldsymbol{r}) >} \tag{15}$$

where $< \boldsymbol{j}_{DC}(\boldsymbol{c},\boldsymbol{r}) >$ and $std\,(\boldsymbol{j}_{DC}(\boldsymbol{c},\boldsymbol{r}))$ denote, respectively, the mean and the standard deviation of the DC current density over the cathode surface. A fully homogeneous distribution would ideally return $CV = 0$.

B. Linking Deposition Uniformity to Radio-Frequency Losses

The radiation efficiency of the resulting antenna after electroplating relies on the quantity and uniformity of the deposited metallic cations over the LIG seed, and, ultimately, on the achieved sheet resistance. Let now $\boldsymbol{J}_{RF}(\boldsymbol{r}, f)$ denote the surface current density locally induced on the electroplated cathode by an electromagnetic source at frequency f. The latter is parametrized as

$$\boldsymbol{J}_{RF}(\boldsymbol{r}, f) = J_0 \boldsymbol{j}_{RF}(\boldsymbol{r}, f) \tag{16}$$

where J_0 is the peak value on the surface of the antenna and $\boldsymbol{j}_{RF}(\boldsymbol{r}, f)$ is the normalized current distribution.

The power dissipated by the cathode due to the resulting ohmic losses is

$$P_j(f) = \frac{1}{2}J_0^2 \int_S R_p(\boldsymbol{c},\boldsymbol{r},T)\,|\boldsymbol{j}_{RF}(\boldsymbol{r},f)|^2\,d\boldsymbol{r} \tag{17}$$

where $R_p(\boldsymbol{c},\boldsymbol{r},T)$ denotes the surface resistance of the LIG-Cu composite. In the early stage of deposition, the deposited layer remains extremely thin, so that the physical thickness of the LIG-Cu complex is significantly lower than the skin depth at the frequency f [37]. Accordingly, the value of R_p is frequency-independent and coincides with the DC one in (11). Thus, (17) reduces to

$$P_j(f) = \frac{R_{s,seed}\boldsymbol{j}_{95}J_0^2}{2} \int_S \frac{|\boldsymbol{j}_{RF}(\boldsymbol{r},f)|^2}{|\boldsymbol{j}_{DC}(\boldsymbol{c},\boldsymbol{r})| + \boldsymbol{j}_{95}} d\boldsymbol{r} \tag{18}$$

C. Optimization algorithm

Let's introduce the following penalty function, $\mathcal{P} \in [0, \inf)$, which is related to both the RF power loss and the uniformity of the deposit:

$$\mathcal{P}(\boldsymbol{c}) = CV(\boldsymbol{c}) \cdot \int_S \frac{|\boldsymbol{j}_{RF}(\boldsymbol{r},f)|^2}{|\boldsymbol{j}_{DC}(\boldsymbol{c},\boldsymbol{r})| + \boldsymbol{j}_{95,max}} d\boldsymbol{r}. \tag{19}$$

Where $\boldsymbol{j}_{95,max}$ denotes the maximum 95th-percentile value of the DC current distribution among all configurations, $\boldsymbol{c}$, ensuring a consistent comparison among all candidate biasing configurations. The penalty function is formulated to bridge the early stage of electrodeposition with the final RF performance: the CV quantifies the uniformity of the initial current distribution and indicates the layouts that are more susceptible to local overgrowth and non-uniform metal deposition, whereas the integral term is proportional to the power dissipation of the electroplated antenna. Moreover, the minimization of this function also prioritizes the deposition in regions where the RF current density is naturally higher, as these areas are more sensitive to insufficient plating thickness. $\mathcal{P}$ can be generalized to a set of Q frequencies to handle broadband or multi-band antennas as

$$\mathcal{P}(\boldsymbol{c}) = CV(\boldsymbol{c}) \cdot \sum_{q=1}^{Q} w_q \int_S \frac{|\boldsymbol{j}_{RF}(\boldsymbol{r},f_q)|^2}{|\boldsymbol{j}_{DC}(\boldsymbol{c},\boldsymbol{r})| + \boldsymbol{j}_{95,max}} d\boldsymbol{r} \tag{20}$$

where w_q are weighting coefficients to selectively account for the different contributions. The penalty function must be minimized with respect to the biasing configuration. For the sake of simplicity, we hereafter assume equal-current biasing

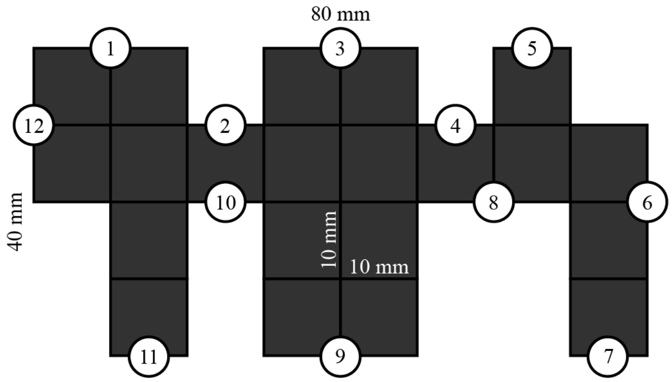

(a)

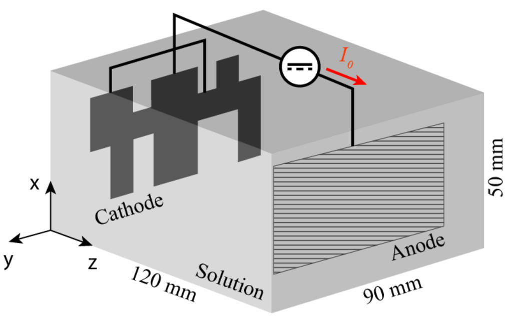

(b)

Fig. 4: Test structure: (a) Layout of the LIG cathode composed of 21 identical 10×10 mm^2 squares. Circles indicate the trial grid of feed points. (b) DC Simulation domain.

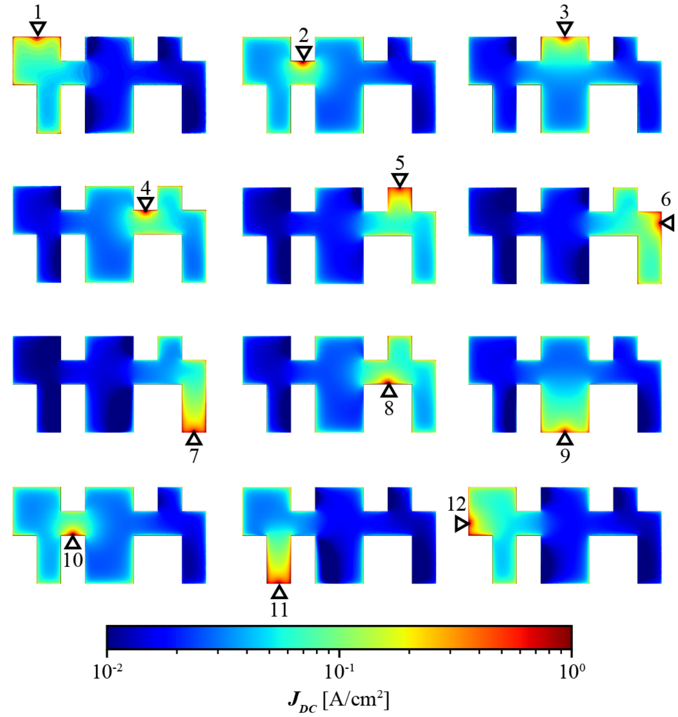

Fig. 5: Test structure: Normalized DC surface current density for different positions of a single bias node (tagged by a triangle).

nodes ($I_n = I/N, \ \forall n$), so that the problem reduces to identifying the most-suitable set of positions, $\{\boldsymbol{r}_i\}$, over a predefined grid on the LIG surface, $\boldsymbol{R'}$.

The optimization proceeds incrementally, selecting at each step a further feed point that, together with the already placed nodes, returns the minimum penalty. Each additional contact, indeed, redistributes the DC current, reduces potential gradients, and improves plating uniformity while mitigating ohmic losses.

Specifically, the position of the m-*th* node is optimized among the remaining positions after having already identified the $(m-1)$-*th* ones, according to the following procedure:

- *step 1*: find the optimal position $\boldsymbol{r'_1}$ that minimizes $\mathcal{P}$ with a single feed;
- *step 2*: determine $\boldsymbol{r}'_2 \in \boldsymbol{R'} - \{\boldsymbol{r'_1}\}$ to minimize $\mathcal{P}$ for the feed couplet in $\{\boldsymbol{r'_1}, \boldsymbol{r'_2}\}$;
- ...
- *step m*: identify the position $\boldsymbol{r'_m} \in \boldsymbol{R'} - \{\boldsymbol{r'_1}, ..., \boldsymbol{r'_{m-1}}\}$ such that the set of feed points in $\{\boldsymbol{r'_1}, ..., \boldsymbol{r'_{m-1}}, \boldsymbol{r'_m}\}$ minimizes $\mathcal{P}$.

This iterative algorithm allows determining the minimum number of biasing points required to achieve a satisfactory uniformity, thereby quantifying the trade-off between added system complexity and the resulting improvement in deposition quality. Notably, the computational effort, $C_i(M)$, associated with this procedure is minimized: when up to $M \leq N$ bias points are optimized, the minimum number of required DC simulations is given by (21)

$$C_i(M) = \sum_{m=0}^{M-1} (N - m) = \frac{M(2N - M + 1)}{2}. \qquad (21)$$

In case all the N considered bias points are evaluated to identify the best configuration, the computational effort reduces to Gauss sum, $C_i(N) = N(N+1)/2$, thus scaling quadratically with N. For comparison, exploring all the possible combinations of $\binom{N}{M}$ bias points, without preserving the intermediate positions, would require an exponential number of simulations, given by $\sum_{m=1}^{M} \binom{N}{M} \to 2^N - 1$.

Additionally, preliminary investigations with more exhaustive yet computationally expensive minimization algorithms returned similar results, as reported in the Supplementary Information.

III. Validation

The optimization procedure is demonstrated and experimentally verified by a challenging electroplating example of a LIG seed (i.e., the cathode) having a modest electrical conductivity ($\sigma_{LIG} = 500 \ S/m$). The geometry, which could resemble that of a shaped patch antenna, is asymmetric, irregular and features slender LIG traces that are expected to induce a non-negligible potential drop between adjacent biasing nodes (Fig. 4a). The plating system (Fig. 4b) also includes a rectangular copper anode spaced 10 cm apart and a plating solution containing copper cations ($\sigma_{sol} = 0.2 \ S/m$). Anode and cathode are biased by a total unitary constant current.

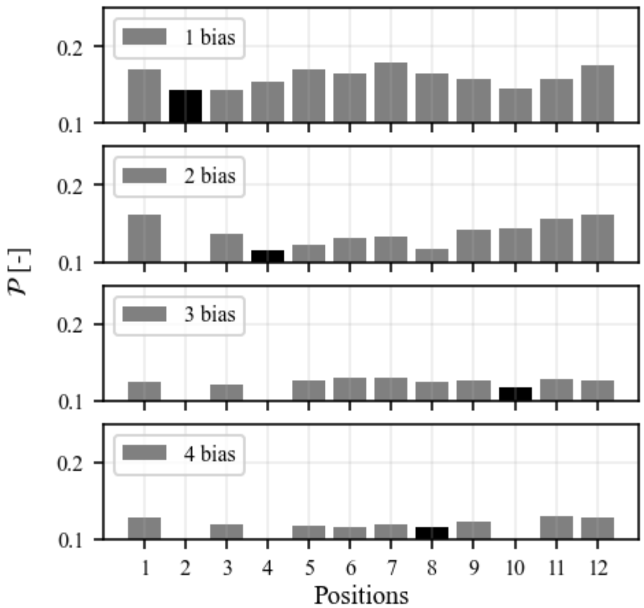

(a)

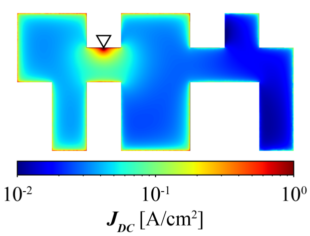

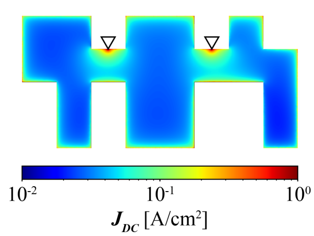

(b) (c)

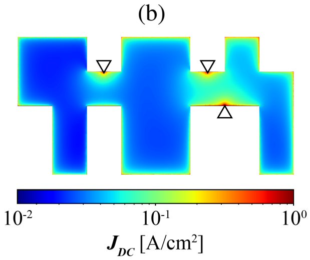

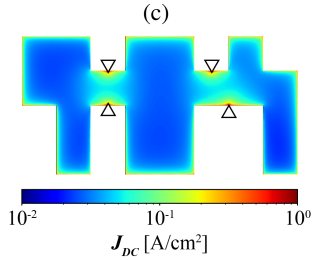

(d) (e)

Fig. 6: Test structure: (a) Penalty functions for each feed positioning. The black bar corresponds to the optimum for that configuration. (b) - (e) Normalized surface current distributions for 1, 2, 3, and 4 optimized sets of feed points.

In this first experiment, we will focus on the plating homogeneity, by assuming a zero RF current ($|\boldsymbol{j}_{RF}(\boldsymbol{r}, f)| = 0\ \forall\ \boldsymbol{r} \in \Psi$). Accordingly, the penalty function (19) reduces to the CV and the measured distribution of sheet resistance in DC will be directly compared to the simulated one by (11). RF losses will be fully considered in the antenna example in the next Section.

The numerical experiment considers incremental combinations of single, double, triple and quadruple biasing points chosen on a grid of $N = 12$ possible positions, $\boldsymbol{R'}$, progressively labeled as $n = 1, ..., 12$ on the cathode perimeter (Fig. 4a).

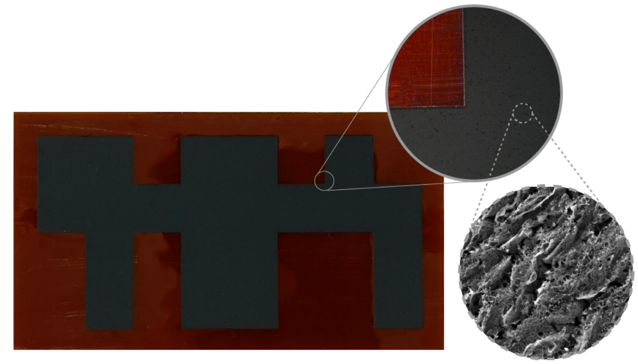

(a)

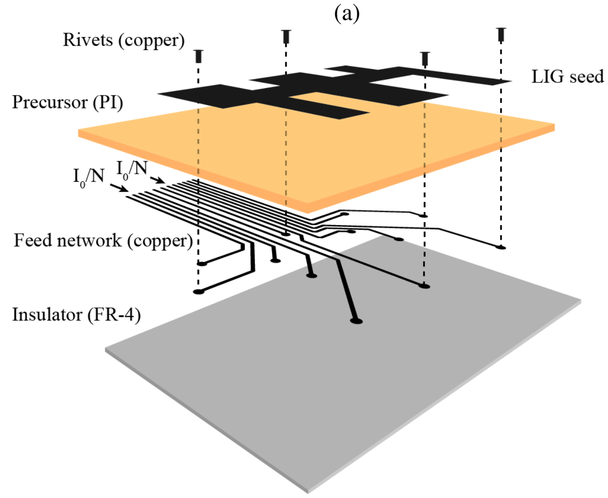

(b)

Fig. 7: Test structure: (a) LIG seed cathode, with stereo-microscope and scanning electron microscope (SEM) magnifications (7x and 2790x) shown in the left and right insets, respectively. (b) Schematic feeding network used to drive DC current to each position on the LIG cathode.

A. Numerical analysis

The Laplace equation (13) is solved for each considered biasing configuration using the Electrostatic Finite Element Method (FEM) solver in CST Microwave Studio 2025. Fig. 5 shows the DC current distribution for all the single-bias positions. The incremental optimization steps are summarized in the histograms of Fig. 6a reporting the penalty functions for each configuration.

For the single-node case, the first optimization step identifies $n = 2$ as the optimal bias position. The penalty function varies by almost 20% across the twelve grid nodes, confirming that the choice of the first feed point is the most critical one.

In the second iteration, the algorithm selects a second bias at $n = 4$, which improves deposition uniformity ($\approx$ 17% improvement) by reducing current crowding. Introducing a third or fourth node does not yield further meaningful reduction but only reduces the variability among different nodes. Overall, two biasing points are hence sufficient for near-optimal uniformity.

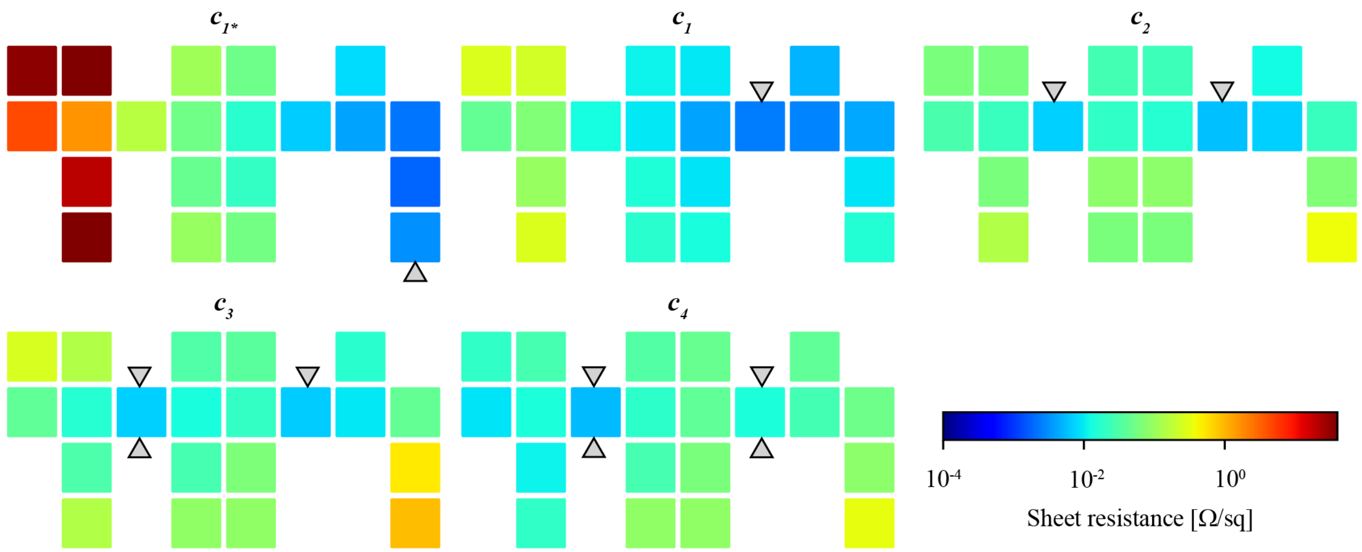

Fig. 8: Test structure: Measured sheet resistance in each sub-region for different biasing configurations. Triangle markers indicate the positions of the bias points.

TABLE II: LASER SETTINGS FOR THE SEED ENGRAVING ON THE CATHODE.

Power $[W]$	**Scan Speed** $[cm/s]$	**Offset** $[mm]$	**Resolution** $[PPI]$
5.1	14.0	-1.5	1000

B. Experimental corroboration

1) Setup preparation: The geometry considered in the numerical model was replicated on PI using CO_2 laser patterning with the settings in Table II (Fig. 7a). The feeding system (Fig. 7b) comprises an FR-4 board hosting a copper biasing network etched by a Mipec 4mill 300ATC drilling machine. The board was attached to the PI film by double-sided tape. The terminal electrodes injecting current into the LIG were connected via metallic rivets, later removed. Cathode and anode (20 cm spaced apart) were immersed in a copper-sulfate solution ($K = 0.4\ \mu\text{m/min} \ @\ 1\ \text{A/dm}^2$) purchased by Dr. Galva [38], and a total current $I_{tot} = 100$ mA was supplied to the feeding network through gator terminals. The experimental campaign compares the optimized configurations $\{\mathbf{c_1}, \mathbf{c_2}, \mathbf{c_3}, \mathbf{c_4}\}$, numerically identified as the best-performing sets for $n = \{2\}$, $n = \{2,\ 4\}$, $n = \{2,\ 4,\ 8\}$, and $n = \{2,\ 4,\ 8,\ 10\}$, respectively, with a worst-case single-bias reference ($\mathbf{c_{1*}}$) placed at $n = 7$, which yielded the lowest uniformity in simulation. All the configurations were tested for $T = 60$ min.

After electroplating, the cathodes were cut into 10×10 mm^2 squares following the scheme in Fig. 4a, and the sheet resistance in each sub-region was measured with a four-point probe system [39]. The experimental results were compared with simulations via the coefficient of variation, CV, now expressed, from (11), in terms of the measurable sheet resistance after plating

$$CV = \frac{std(R_s(x,y))}{< R_s(x,y) >} \tag{22}$$

where (x, y) denote sub-region coordinates.

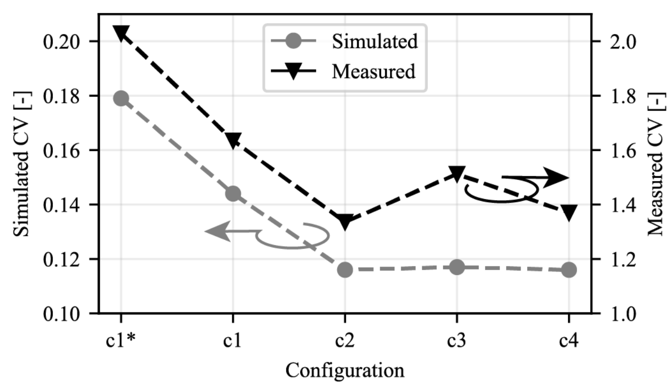

Fig. 9: Test structure: Simulated (gray circle) and measured (black triangle) CV for different tested configurations

2) Results: Fig. 8 shows the sheet resistance maps over the surface of the cathodes after electroplating; Fig. 9, instead, compares the simulated and measured CV. Configuration $\mathbf{c_{1*}}$ returns the highest coefficient of variation due to the current crowding near to the bias point, and the small current density in the opposite region. Consequently, the sheet resistance drops to approximately 10 mΩ/sq in the lower-right corner of the cathode, whereas it remains close to that of the seed ($R_s \approx 40\ \Omega$/sq) on the left side.

Optimizing the position of the single bias point ($\mathbf{c_1}$) significantly improves the deposition uniformity, even if a sheet-resistance difference of approximately one order of magnitude is still observed between the left and right sides of the cathode. The lowest CV is achieved with configuration $\mathbf{c_2}$, where

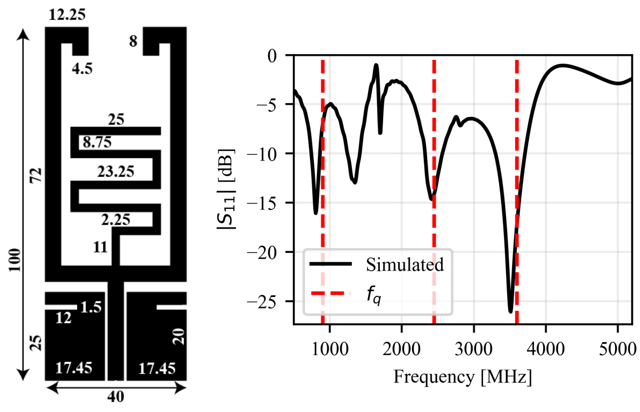

(a) (b)

Fig. 10: Tri-band antenna: (a) Layout. Size $[\mathrm{mm}]$. (b) Simulated reflection coefficient.

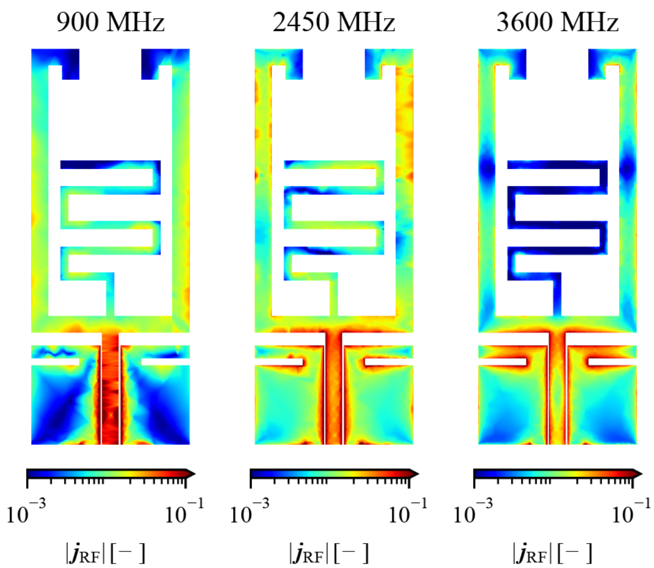

(a) (b) (c)

Fig. 11: Tri-band antenna: normalized RF surface current distribution.

two optimally positioned bias points reduce both the average sheet resistance and its variability to approximately 60 and 80 $\mathrm{m}\Omega/\mathrm{sq}$, respectively. Further increasing the number of bias points ($\mathbf{c_3}$ and $\mathbf{c_4}$) does not produce any significant improvement due to asymmetries in the potential distribution and current dilution.

Finally, it is worth noting that the good trend agreement between the simulated and measured CV confirms that the ranking prediction of the different configurations by the early-stage analysis is preserved even after prolonged electrodeposition, and that the penalty function remains reliable throughout the deposition process.

IV. Application to a tri-band IoT antenna

The method is now applied to a tri-band monopole antenna (Fig. 10a), derived from [40], that combines a coplanar microstrip feedline, a U-shaped conductor, and an internal meandered section, and operates at 900, 2450, and 3600 MHz.

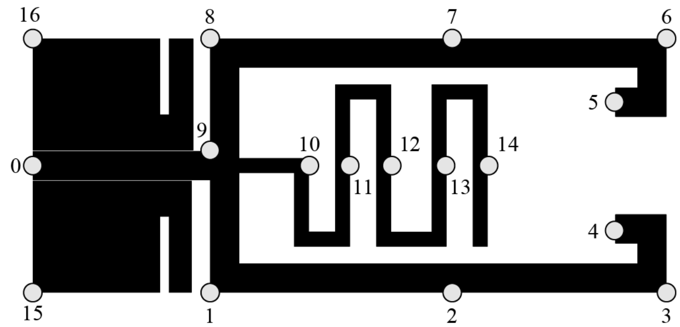

Fig. 12: Tri-band antenna: grid of the trial biasing nodes

The use of a well-established yet challenging layout allows quantifying the practical benefit of the optimized electroplating configuration while separating electroplating-induced effects from purely electromagnetic design choices. The selected geometry includes slender serpentine traces, narrow gaps, partially disconnected regions, and high-aspect-ratio current paths. These features amplify terminal effects on low-conductivity LIG seeds, making the structure prone to non-uniform deposition and unintended short-circuiting. Accordingly, the resulting antenna performance is primarily determined by the adopted biasing configuration rather than by the antenna geometry itself.

The LIG seed is engraved on a PI film ($\epsilon = 3.5,\ tan(\delta) = 27 \cdot 10^{-3}$) laminated on a Poly-methyl-methacrylate (PMMA) slab ($\epsilon = 2.6,\ tan(\delta) = 9 \cdot 10^{-3}$, $0.8\ \mathrm{mm}$ thick) to ensure mechanical rigidity. The corresponding simulated reflection coefficient is reported in Fig. 10b.

The RF current density, $|j_{RF}(\boldsymbol{r}, f)|$ (Fig. 11), computed by the Finite-Difference Time-Domain (FDTD) solver in CST Studio, is mainly concentrated along the microstrip line, especially at lower frequencies. The tri-band response is generated by the sequence of resonance and anti-resonance profiles occurring on the U-shaped element. The meandered trace contributes to radiation mainly at 900 MHz and 2450 MHz, while it remains nearly inactive at the highest frequency. The axial ratio values in the broadside direction ($15 < AR < 40$) indicate a linearly polarization at each frequency of interest.

A. Optimization

The optimization algorithm considers a grid of 17 candidate biasing positions placed along the antenna perimeter (Fig. 12). The contributions of the three frequencies have been equally weighted ($w_1 = w_2 = w_3 = 1/3$). Further tests with non-uniform weighting produced similar allocation of bias points, and are not reported here for brevity.

For a single bias point, the penalty function (Fig. 13) exhibits more than two orders of magnitude variation depending on the node position. The minimum occurs at n=0, located on the microstrip feedline where the RF current density is maximum and where non-uniform plating would have the largest RF impact. The farthest positions from the feedline

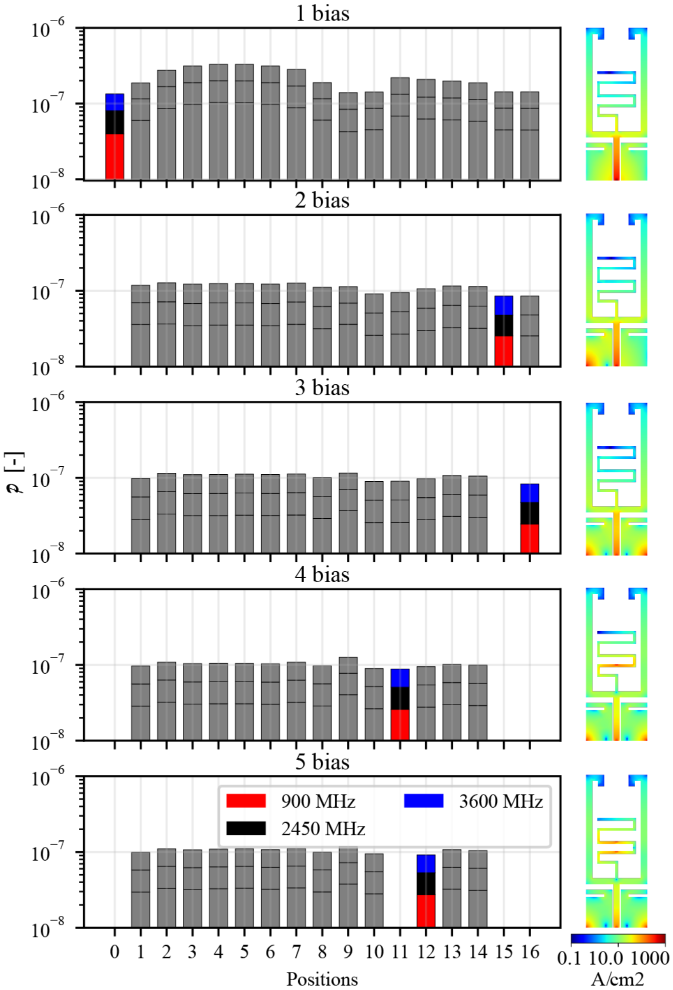

Fig. 13: Tri-band antenna: Penalty function for the sets of 1, 2, 3, 4, and 5 biasing nodes computed as the weighted sum of the single contributions at 900 MHz (red), 2450 MHz (black), and 3600 MHz (blue). Corresponding static current distribution on the left.

($n = 4$ and $n = 5$) yield the highest penalty as RF-relevant regions ($n = \{0,\ 9,\ 10,\ 15,\ 16\}$) remain nearly unplated. Introducing a second node decreases the local minimum of the penalty function by 50% w.r.t. the single-node configuration, but for $n = 3$, $\mathcal{P}$ reaches its minimum. The monotonic decrease of the CV (Fig. 14) confirms that adding feed points always improves the spatial uniformity of the deposition. The penalty, instead, exhibits a minimum (for three points) because it also accounts for the strong non-uniformity of the RF surface currents: when too many feed points are used, the DC current is uniform but excessively diluted and, in turn, the growth-rate in the regions that are most relevant for antenna operation becomes slower. As a consequence, for a fixed deposition duration, the resistivity of these areas is still high, and the ohmic dissipation at RF is significant. Conversely, when the position of the electrical contacts is strategically selected, as for $\mathbf{c_3}$, the plating process jointly maximizes the uniformity and minimizes ohmic losses at RF. For sufficiently long plating times this effect disappears, and

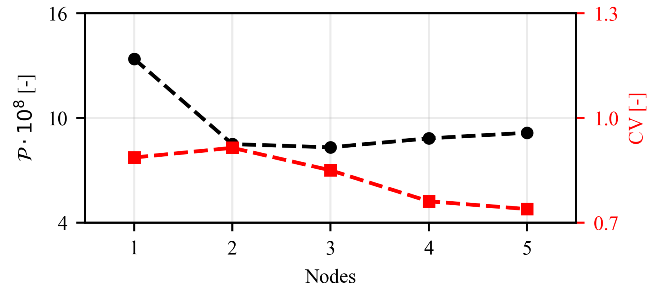

Fig. 14: Minimum of $\mathcal{P}$ (black) and corresponding CV (red) versus the optimized set of nodes.

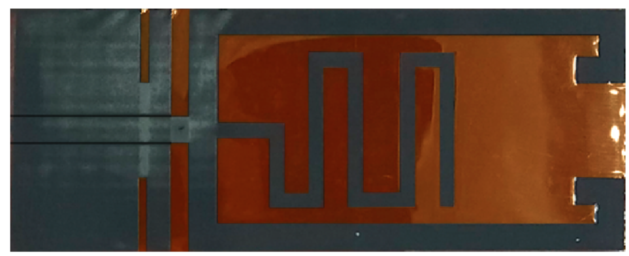

Fig. 15: Tri-band antenna: photo of the LIG seed layer

additional feed points become beneficial again. The penalty minimum therefore identifies the most-suitable configuration balancing morphological uniformity, current dilution, and RF loss reduction within the available electroplating time.

It is also worth noting that the contributions of the three frequencies $\{900,\ 2450,\ 3600\}$ MHz become comparably weighted in the penalty function, indicating that the optimized configuration simultaneously addresses all operating bands.

B. Prototype & test

Three configurations were fabricated:

- $\mathbf{c_1}$: single-bias configuration (optimal one-node placement on the microstrip);
- $\mathbf{c_3}$: optimized three-bias configuration (microstrip + two ground-plane corners).
- $\mathbf{c_5}$: optimized five-bias configuration (microstrip + two ground-plane corners + dual-contact at the meandered trace center).

Electroplating was carried out with the same solution as in Section III using $I_{tot} = 100$ mA. Three plating durations were selected: $T = \{30,\ 60,\ 120\}$ min. After plating, the structure was connected to an SMA connector for RF measurements. Fig. 15 shows the LIG seed pattern, the electroplated antennas, and microscope close-ups highlighting the details of the deposition even inside very narrow gaps.

1) Visual Morphology and Electrical Continuity: For $T =$ 30 min, all configurations show partial plating, but in case of $\mathbf{c_1}$ only the region near the feed is coated and half of the ground plane is plated despite the lack of an electrical connection to the bias network. Magnifications reveal that the latter is short-circuited to the microstrip even for such rapid deposition. This is due to the high current density close to

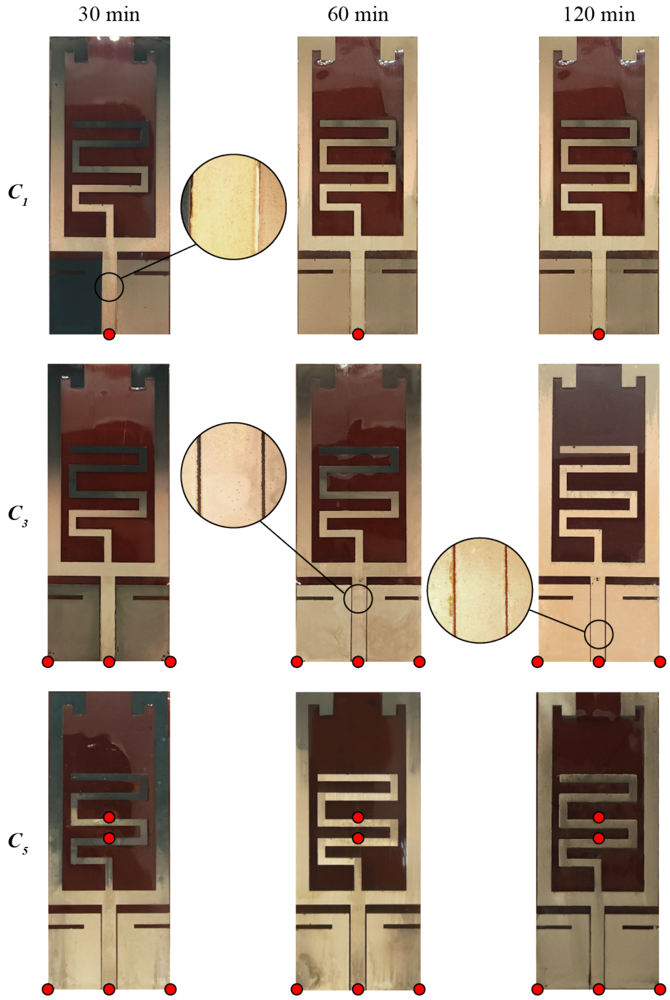

Fig. 16: Tri-band antenna: the prototypes of $\mathbf{c_1}$ (optimal 1 bias point), $\mathbf{c_3}$ (optimal 3 bias points), and $\mathbf{c_5}$ (optimal 5 bias points) configurations after 30 min, 60 min, and 120 min depositions. 7x magnifications of the narrow microstrip-ground plane gaps in the insets. Red dots indicate the positions of the biasing nodes.

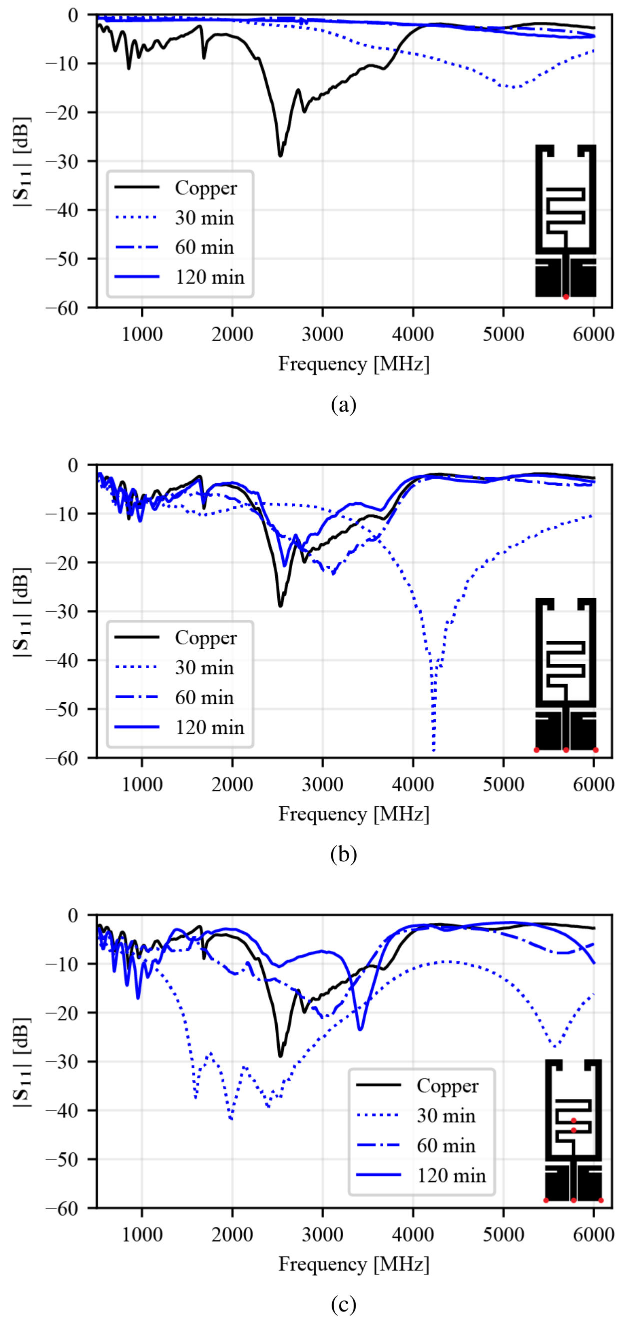

Fig. 17: Tri-band antenna: measured reflection coefficients for (a) $\mathbf{c_1}$, (b) $\mathbf{c_3}$, and (c) $\mathbf{c_5}$ after 30 min (dot), 60 min (dash), and 120 min (solid) deposition.

the single-bias point, especially at the edges of the trace, that causes an overgrowth of the deposit, bridging of the gap, and, in turn, a short circuit. For $\mathbf{c_3}$ and $\mathbf{c_5}$ configurations, instead, plating safely extends to both ground halves; slot isolation is preserved, and no shorting is detected.

After 60 minutes, the overall copper coverage becomes more extended for both configurations. In $\mathbf{c_1}$, the plating spreads across a larger portion of the structure but remains visibly non-uniform, and copper accumulates also inside the two microstrip gaps. In contrast, neither $\mathbf{c_3}$ and $\mathbf{c_5}$ exhibits signs of local overgrowth, with the latter producing the most uniform and well-balanced deposition, as expected.

After 120 minutes, the entire LIG pattern is fully coated in both cases; however, the resulting morphologies differ substantially. In $\mathbf{c_1}$, the excessive local growth near the feed point completely fills the narrow gaps separating the microstrip from the ground plane. Conversely, $\mathbf{c_3}$ and $\mathbf{c_5}$ achieve full and uniform coverage and all geometrical discontinuities, including the microstrip gap and the meandered sections, remain intact.

2) Reflection coefficient measurement: Reflection-coefficient measurements were carried out by Vector Network Analyzer (Keysight P9377B) for the three plating durations and compared against the bulk-copper reference, sharing the same geometrical features and assembly procedure.

Fig. 17 and 18 report the measured amplitude and phase of the S_{11}, respectively, and compare them with the copper reference. For the single-bias configuration $\mathbf{c_1}$, the antenna

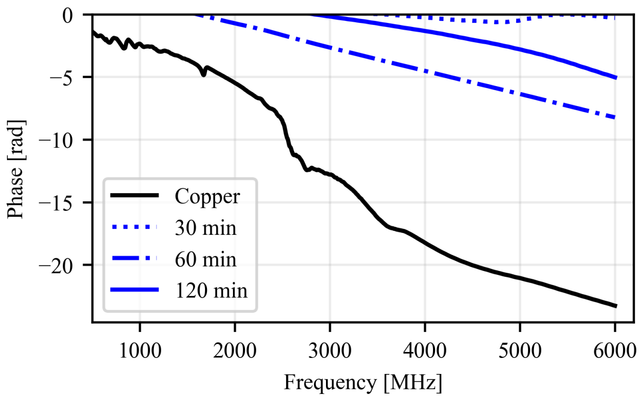

(a)

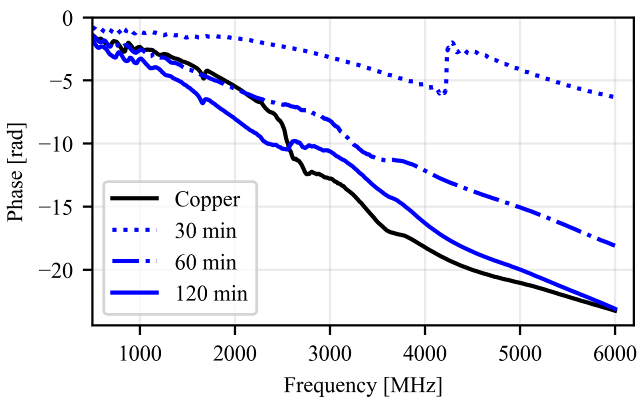

(b)

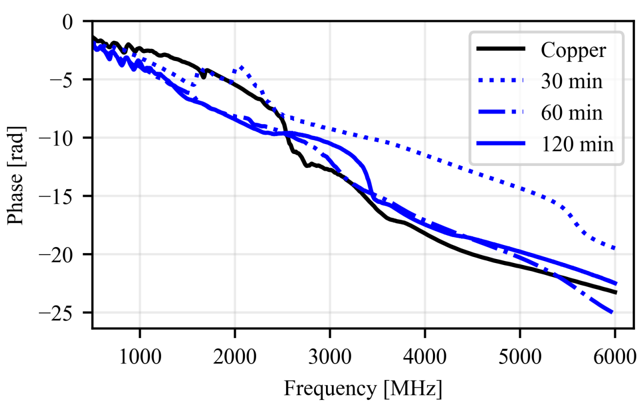

(c)

Fig. 18: Tri-band antenna: measured phase of the reflection coefficients for (a) $\mathbf{c_1}$, (b) $\mathbf{c_3}$, and (c) $\mathbf{c_5}$ after 30 min (dot), 60 min (dash), and 120 min (solid) deposition.

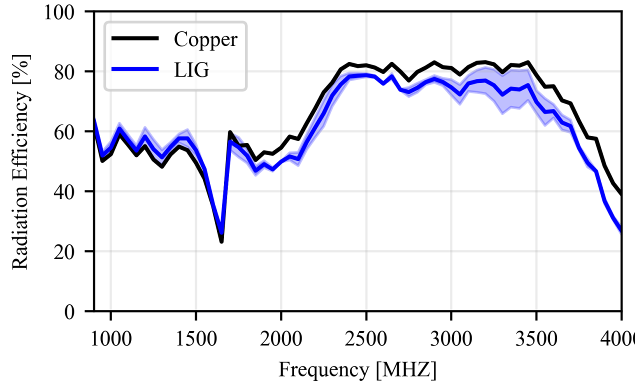

(a)

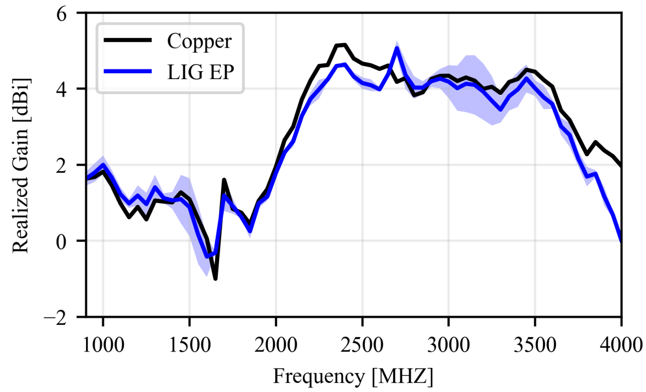

(b)

Fig. 19: Tri-band antenna: comparison of the (a) radiation efficiency and (b) maximum realized gain for the bulk-copper and 3 electroplated-LIG prototypes. Dashed region identifies the dispersion on the three electroplated antennas.

response never approaches that of the copper prototype. Across all deposition times the resonant features appear shifted, weaker, and progressively degraded. After 120 minutes, the S_{11} trace collapses into the characteristic profile of a near-DC short, fully consistent with the slot bridging.

In contrast, after 60 minutes, both $\mathbf{c_3}$ and $\mathbf{c_5}$ already closely follow the copper reference. For longer deposition durations, however, the behavior of the two configurations diverges. After 120 minutes, the amplitude response of $\mathbf{c_3}$ becomes almost indistinguishable from that of the full-copper antenna, indicating that the electroplated structure has reached a plating quality and electrical continuity comparable to bulk metal. In contrast, the module of the reflection coefficient of $\mathbf{c_5}$ does not fully overlap with the copper reference even after $T = 120$ min, showing that the increased number of bias nodes does not translate into a clear RF improvement despite the enhanced morphological uniformity.

3) Efficiency and Radiation pattern: To assess fabrication reproducibility, three replicas of the optimized three-bias configuration were fabricated using the same laser engraving and electroplating procedure. The radiation characteristics of the optimized electroplated antenna were experimentally evaluated using the Spherical Near-Field measurement system (SG EVO

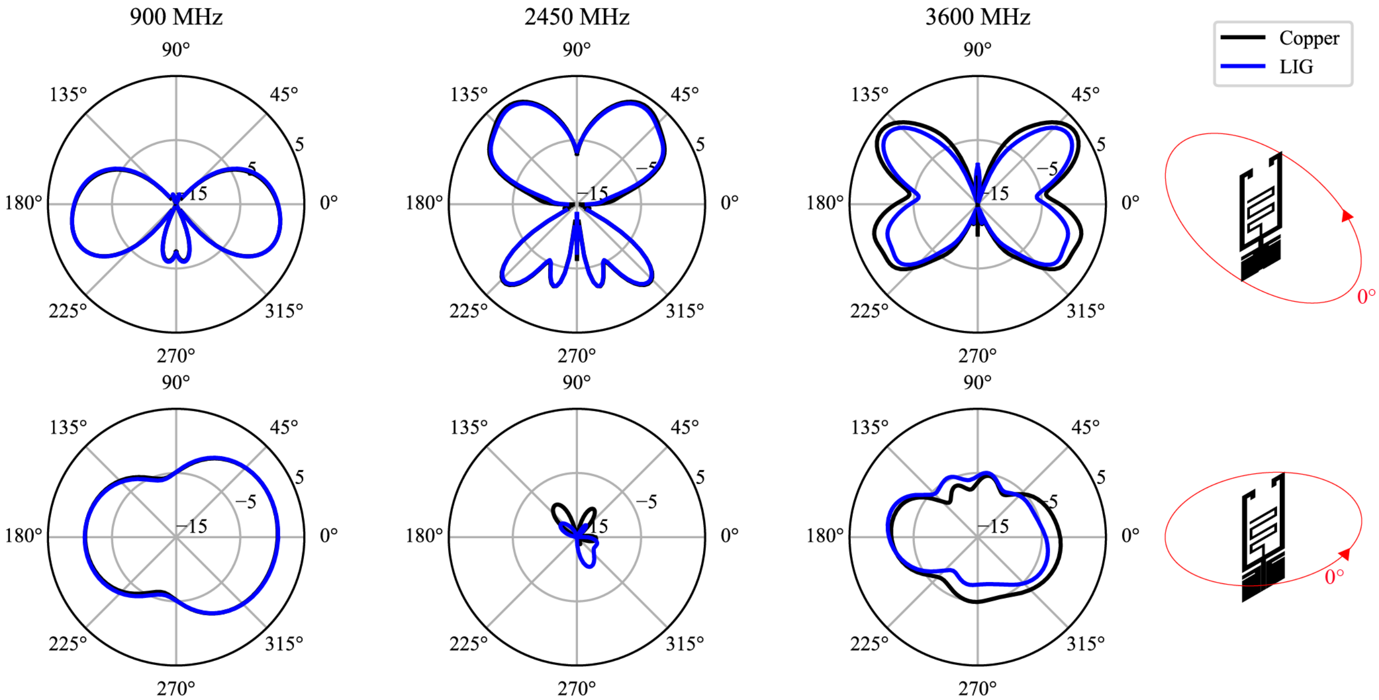

Fig. 20: Tri-band antenna: measured radiation patterns of the LIG (blue) and copper reference (black) antenna on the E-cut (top) and H-cut (bottom).

DP 400-6000 by Microwave Vision Group). The radiation efficiency[1] (Fig. 19a), the radiation patterns on the E- and H-cut planes (Fig. 20), and the maximum realized gain (Fig. 19b) of the three electroplated samples are in strong agreement with the copper reference and exhibit good repeatability across the entire measured band, with an inter-sample variability below 1 dB. The resulting efficiencies for the electroplated prototypes range between 60% and 80% ($\approx -2\ dB$), with values nearly indistinguishable from those of the bulk-copper reference demonstrating that the optimized three-bias configuration produces a surface morphology dense and uniform enough to minimize losses.

V. Conclusions

This work introduced a methodology to achieve homogeneous electroplating starting from low-conductivity LIG seed layers.

A major outcome is that the overall improvement is mostly related to the solution of the first bias point, as the feed-point location strongly influences the DC current distribution and, consequently, the uniformity of the deposited layer. A single feed, however well placed, may remain insufficient for geometries featuring narrow gaps, intricate meanders, or disconnected regions that are difficult to reach with a single current injection. Additional bias points further enhance homogeneity and prevent short circuits even in the presence of sub-millimetre gaps, enabling a complete and uniform build-up of the metallic coating. However, the results demonstrate that increasing the number of bias nodes beyond the best-performing configuration does not necessarily improve RF performance. While the coefficient of variation decreases monotonically, the introduced penalty function exhibits a minimum, indicating that unnecessary current redistribution can slow down metal growth in RF-critical regions and temporarily increase ohmic losses. Therefore, the proposed framework identifies the minimum number of bias points required to achieve RF performance comparable to that of metallic antennas while avoiding unnecessarily complex biasing systems.

The experimental results further corroborate these findings. Although configurations with a larger number of bias nodes exhibit improved morphological uniformity, the RF response does not necessarily benefit from the additional contacts. In particular, the optimized three-bias configuration converges to the copper reference after sufficiently long deposition times, whereas the five-bias configuration does not provide a clear RF advantage despite the more uniform plating. This result confirms that the proposed method can determine not only the minimum number of nodes, but also their physically meaningful placement, even for antennas with complex shapes and multiple resonant modes.

Acknowledgment

The authors wish to thank Francesco Mancuso, and Camilla Medori, and Dr. Jaydeep Singh (Microwave Vision Group), and Dr. Andrea Giacomini (Microwave Vision Group) for valuable technical and scientific support.

The authors used artificial intelligence (AI)–assisted tools (ChatGPT) to support language editing and/or text refinement. The authors take full responsibility for the content of this manuscript.

[1]radiation efficiency η_R is derived from the measured total efficiency, e_0, and subtracting the mismatch losses $\eta_R = e_0/(1-|S_{11}|^2)$.

References

[1] D. Helena, A. Ramos, T. Varum, and J. N. Matos, "Antenna design using modern additive manufacturing technology: A review," *IEEE Access*, vol. 8, pp. 177064–177083, 2020.

[2] L. Ji, S. Wang, C. Wang, G. Chen, Y. Chen, W. He, and Z. Tan, "Improved uniformity of conformal through-hole copper electrodeposition by revision of plating cell configuration," *Journal of The Electrochemical Society*, vol. 162, no. 12, p. D575, 2015.

[3] T. M. Abdel-Fattah, J. D. Loftis, and A. K. Mahapatro, "Nanoscale electrochemical polishing and preconditioning of biometallic nickel-titanium alloys," *Nanoscience and Nanotechnology*, vol. 5, pp. 36–44, 2015.

[4] J. M. Platt, L. B. Boskovic, and D. S. Filipovic, "Wideband biconical antenna with embedded band-notch resonator," *IEEE Transactions on Antennas and Propagation*, vol. 72, no. 3, pp. 2921–2925, 2024.

[5] B. Zhang, J. Ren, T. Yang, Y.-T. Liu, Z. Zhao, J. Zhao, Y. Liu, and Y. Yin, "Three-port pattern-and polarization-diversity rectangular dielectric resonator antenna," *IEEE Transactions on Antennas and Propagation*, vol. 71, no. 6, pp. 5392–5397, 2023.

[6] Z. L. Ma and X. F. Xiao, "Additively manufactured dual circularly polarized antennas with bidirectional same-sense radiation and wide bandwidth characteristics," *IEEE Transactions on Antennas and Propagation*, vol. 71, no. 1, pp. 1029–1034, 2022.

[7] B.-J. Chen, H. Yi, K. B. Ng, S.-W. Qu, and C. H. Chan, "3d printed reflectarray antenna at 60 ghz," in *2016 International symposium on antennas and propagation (ISAP)*, pp. 92–93, IEEE, 2016.

[8] Z. L. Ma, S. C. Peng, Q.-X. Chu, and Q. Xue, "3-d printed annular linear-to-circular dielectric polarizer and its applications to omnidirectional and multibeam antennas," *IEEE Transactions on Antennas and Propagation*, vol. 70, no. 10, pp. 9365–9375, 2022.

[9] R. Bowrothu, H.-I. Kim, S. Hwangbo, and Y. K. Yoon, "High-radiation efficiency in array antennas using cu/co metaconductors," *IEEE Transactions on Antennas and Propagation*, vol. 69, no. 11, pp. 7993–7998, 2021.

[10] H. Rmili, O. El Mrabet, J.-M. Floc'h, and J.-L. Miane, "Study of an electrochemically-deposited 3-d random fractal tree-monopole antenna," *IEEE transactions on antennas and propagation*, vol. 55, no. 4, pp. 1045–1050, 2007.

[11] M. Meissner, N. Spengler, D. Mager, N. Wang, S. Kiss, J. Höfflin, P. While, and J. Korvink, "Ink-jet printing technology enables self-aligned mould patterning for electroplating in a single step," *Journal of Micromechanics and Microengineering*, vol. 25, no. 6, p. 065015, 2015.

[12] Y.-S. Eom, J.-H. Son, H.-S. Lee, K.-S. Choi, H.-C. Bae, J.-Y. Choi, T.-S. Oh, and J.-T. Moon, "Development of copper electro-plating technology on a screen-printed conductive pattern with copper paste," *Journal of the Microelectronics and Packaging Society*, vol. 22, no. 1, pp. 51–54, 2015.

[13] N. Lazarus, S. S. Bedair, S. H. Hawasli, M. J. Kim, B. J. Wiley, and G. L. Smith, "Selective electroplating for 3d-printed electronics," *Advanced Materials Technologies*, vol. 4, no. 8, p. 1900126, 2019.

[14] K. A. Ohiri, N. M. Nowicki, T. J. Montalbano, M. Presley, and N. S. Lazarus, "Electroplating of aerosol jet-printed silver inks," *Advanced Engineering Materials*, vol. 23, no. 10, p. 2100362, 2021.

[15] L.-p. Wu, J.-j. Zhao, Y.-p. Xie, and Z.-d. Yang, "Progress of electroplating and electroless plating on magnesium alloy," *Transactions of Nonferrous Metals Society of China*, vol. 20, pp. s630–s637, 2010.

[16] V. Fiodorov, K. Ratautas, Z. Mockus, R. Trusovas, L. Mikoliūnaitė, and G. Račiukaitis, "Laser-assisted selective fabrication of copper traces on polymers by electroplating," *Polymers*, vol. 14, no. 4, p. 781, 2022.

[17] Y. Chyan, R. Ye, Y. Li, S. P. Singh, C. J. Arnusch, and J. M. Tour, "Laser-induced graphene by multiple lasing: toward electronics on cloth, paper, and food," *ACS nano*, vol. 12, no. 3, pp. 2176–2183, 2018.

[18] A. Mostaccio and G. Marrocco, "Laser-induced graphene: A green technology for the iot," *IEEE Electron Devices Magazine*, vol. 2, no. 2, pp. 11–22, 2024.

[19] J.-H. Han, S. H. Park, S. Kim, and J. J. Pak, "A performance improvement of enzyme-based electrochemical lactate sensor fabricated by electroplating novel pdcu mediator on a laser induced graphene electrode," *Bioelectrochemistry*, vol. 148, p. 108259, 2022.

[20] S.-F. Tseng, J.-W. Huang, C.-C. Lee, and C.-C. Kuo, "Highly sensitive and flexible strain sensors based on electroplating copper/laser-induced graphene composites," *Journal of Alloys and Compounds*, vol. 1022, p. 179928, 2025.

[21] M. Chang, R. Tang, W. Zou, J. Xian, Z. Zhang, X. Liu, M. Qu, and C. Zhang, "A high-performance phosphate potentiometric sensor based on cobalt nanoparticles electroplated on hierarchically porous laser-induced graphene," *Advanced Materials Interfaces*, vol. 11, no. 15, p. 2301111, 2024.

[22] S. Jeong, S. Yang, Y. J. Lee, and S. H. Lee, "Laser-induced graphene incorporated with silver nanoparticles applied for heavy metal multi-detection," *Journal of Materials Chemistry A*, vol. 11, no. 25, pp. 13409–13418, 2023.

[23] A. Lazaro, M. R. Cujilema, R. Villarino, M. Lazaro, and D. Girbau, "A novel approach for wine anti-counterfeiting using laser-induced graphene chipless rfid tags on cork," *Scientific Reports*, vol. 15, no. 1, p. 12750, 2025.

[24] S. Armini and P. M. Vereecken, "Impact of" terminal effect" on cu plating: theory and experimental evidence," *ECS Transactions*, vol. 25, no. 27, p. 185, 2010.

[25] D. M. De Leeuw, P. Kraakman, P. Bongaerts, C. Mutsaers, and D. Klaassen, "Electroplating of conductive polymers for the metallization of insulators," *Synthetic metals*, vol. 66, no. 3, pp. 263–273, 1994.

[26] A. Mostaccio, F. Mancuso, and G. Marrocco, "Electroplating for flexible antennas by using laser-induced graphene masks," in *2025 19th European Conference on Antennas and Propagation (EuCAP)*, pp. 1–4, IEEE, 2025.

[27] S.-H. Yu, C.-P. Kao, C.-W. Ma, J.-K. Fang, P.-F. Yang, and H.-C. Chang, "Application of the taguchi method to minimize the non-uniformity of copper deposition in electroplating with numerical model," *Journal of the Taiwan Institute of Chemical Engineers*, vol. 156, p. 105379, 2024.

[28] A. Mahapatro and S. K. Suggu, "Modeling and simulation of electrodeposition: Effect of electrolyte current density and conductivity on electroplating thickness," *Adv. Mater. Sci*, vol. 3, no. 2, p. 1, 2018.

[29] N. Obaid, R. Sivakumaran, J. Lui, and A. Okunade, "Modelling the electroplating of hexavalent chromium," in *COMSOL Conference. Boston2013*, 2013.

[30] G. Yang, D. Deng, Y. Zhang, Q. Zhu, and J. Cai, "Numerical optimization of electrodeposition thickness uniformity with respect to the layout of anode and cathode," *Electrocatalysis*, vol. 12, no. 5, pp. 478–488, 2021.

[31] N. Ishizuka, T. Yamada, K. Izui, and S. Nishiwaki, "Topology optimization for unifying deposit thickness in electroplating process," *Structural and Multidisciplinary Optimization*, vol. 62, no. 4, pp. 1767–1785, 2020.

[32] H. Deligiannia, J. Dukovica, and S. Mehdizadeh, "Computational aspects of the terminal effect on wafer-scale uniformity," in *Tutorials in Electrochemical Engineering–mathematical Modeling: Proceedings of the International Symposium*, vol. 99, p. 124, The Electrochemical Society, 1999.

[33] E. Broadbent, E. McInerney, L. Gochberg, and R. Jackson, "Experimental and analytical study of seed layer resistance for copper damascene electroplating," *Journal of Vacuum Science & Technology B: Microelectronics and Nanometer Structures Processing, Measurement, and Phenomena*, vol. 17, no. 6, pp. 2584–2595, 1999.

[34] K. M. Takahashi, "Electroplating copper onto resistive barrier films," *Journal of the Electrochemical Society*, vol. 147, no. 4, p. 1414, 2000.

[35] T. Sharma, P. Shaver, D. A. Brown, R. Brüning, V. Peldzinski, and A. Ferro, "Time evolution of stress and microstructure in electroplated copper films," *Electrochimica Acta*, vol. 196, pp. 479–486, 2016.

[36] S. J. Hearne and J. A. Floro, "Mechanisms inducing compressive stress during electrodeposition of ni," *Journal of applied physics*, vol. 97, no. 1, 2005.

[37] A. Mostaccio, D. Kilani, G. Marrocco, and M. H. Zarifi, "Impedance characterization of laser-induced graphene (lig) at x and ku bands for low-profile and flexible microwave structures," *IEEE Transactions on Microwave Theory and Techniques*, 2025.

[38] D. Galva, "Copper plating solution alkaline - for acid-sensitive materials."

[39] F. M. Smits, "Measurement of sheet resistivities with the four-point probe," *Bell System Technical Journal*, vol. 37, no. 3, pp. 711–718, 1958.

[40] S.-L. Zuo, Z.-Y. Zhang, and J.-W. Yang, "Planar meander monopole antenna with parasitic strips and sleeve feed for dvb-h/lte/gsm850/900 operation in the mobile phone," *IEEE Antennas and Wireless Propagation Letters*, vol. 12, pp. 27–30, 2012.